

# First Observations of SO<sub>2</sub> from the Satellite Suomi NPP OMPS: Widespread Air Pollution Events over China

Kai Yang<sup>1,2</sup>, Russell R. Dickerson<sup>1</sup>, Simon A. Carn<sup>3</sup>, Cui Ge<sup>4</sup>, and

Jun Wang<sup>4</sup>

---

Corresponding author: Kai Yang, Atmospheric Chemistry and Dynamics Laboratory, Code 614, NASA Goddard Space Flight Center, 8800 Greenbelt Rd Greenbelt, MD 20771, USA.  
(Kai.Yang-1@nasa.gov)

<sup>1</sup>Department of Atmospheric and Oceanic  
Science, University of Maryland College  
Park, College Park, MD 20742, USA.

<sup>2</sup>Atmospheric Chemistry and Dynamics  
Laboratory, NASA Goddard Space Flight  
Center, Greenbelt, MD 20771, USA.

<sup>3</sup> Department of Geological and Mining  
Engineering and Sciences, Michigan

This article has been accepted for publication and undergone full peer review but has not been through the copyediting, typesetting, pagination and proofreading process, which may lead to differences between this version and the Version of Record. Please cite this article as doi: 10.1002/grl.50952

Severe smog episodes over China in January 2013 received worldwide attention. This air pollution was distinguished by heavy loadings of fine particulate matter and SO<sub>2</sub>. To characterize these episodes, we employed the Ozone Mapping and Profiler Suite, Nadir Mapper (OMPS NM), a UV spectrometer flying on the Suomi National Polar-orbiting Partnership (SNPP) spacecraft since October 2011. We developed an advanced algorithm to quantify SO<sub>2</sub> in the lower troposphere, and achieved high quality retrievals from OMPS NM, which are characterized by high precision,  $\sim 0.2$  Dobson Units (DU; 1 DU =  $2.69 \times 10^{16}$  molecules/cm<sup>2</sup>) for instantaneous field of view SO<sub>2</sub> data, and low biases (within  $\pm 0.2$  DU). Here we report SO<sub>2</sub> retrievals and UV aerosol index data for these pollution events. The SO<sub>2</sub> columns and the areas covered by high pollutant concentrations are quantified; the results reveal for the first time the full extent (an area of  $\sim 10^6$  km<sup>2</sup> containing up to 60 kt of SO<sub>2</sub>) of these episodes.

---

Technological University, Houghton, MI  
49931, USA.

<sup>4</sup>Department of Earth and Atmospheric  
Sciences, University of Nebraska Lincoln,  
Lincoln, NE, 68588, USA

## 1. Introduction

The recent winter air pollution episodes over China, as publicized by news reports of sustained dense smog that engulfed Beijing in January 2013, are among the worst in history, rivaling the deadly Great Smog of London in 1952 [Thorsheim, 2009] and the suffocating photochemical smog of Los Angeles [Haagen-Smit, 1952] in the 1940s to 1970s. The largest sources of air pollutants in China are coal combustion and motor vehicle exhausts [He *et al.*, 2002], which respectively were also the major culprits of the historical London and LA smogs. China's fast growing economy, as evidenced by its rapid industrialization and urbanization, is predominantly powered by its abundant supplies of coal, which accounts for about 70 percent of China's total energy consumption [U.S. Energy Information Administration, 2012]. In addition to greenhouse gas (carbon dioxide, CO<sub>2</sub>) emission, coal burning releases significant amounts of air pollutants, including sulfur dioxide (SO<sub>2</sub>), nitrogen oxides (NO<sub>x</sub> = NO + NO<sub>2</sub>), carbon monoxide (CO), mercury (Hg), and fine particles (i.e., smoke). The gaseous pollutants, SO<sub>2</sub> and NO<sub>x</sub>, are usually oxidized in the air and combine with water vapor to form sulfuric and nitric acid aerosols, which may be further mixed with the emitted smoke, ammonia, as well as dust from the deserts of Mongolia and China; this type of mixture is usually the main component of winter smog over eastern China [Tao *et al.*, 2012].

Anthropogenic SO<sub>2</sub> is the key signature of air pollution in China, and its column density serves as a proxy for the concentration of pollutants co-emitted from fossil fuel combustion. This is especially true in the winter months, when relatively low-tech heating by burning coal contributes a large proportion of air pollutants. These pollutants are usually

released into the planetary boundary layer (PBL), but may be subsequently lofted into the free troposphere by the winter cold fronts from the Siberian high [Wang *et al.*, 2003; Dickerson *et al.*, 2007], and transported over long distances [Hsu *et al.*, 2012]. A synoptic perspective on the severity and extent of air pollution can be obtained using space-borne ultraviolet (UV) instruments, capable of detecting its signature component, SO<sub>2</sub>, in the lower atmosphere [Eisinger and Burrow 1998; Krotkov *et al.*, 2006; Carn *et al.*, 2007; Lee *et al.*, 2008; Nowlan *et al.*, 2011] and providing daily global coverage to monitor its evolution and transport. In this paper we report the first SO<sub>2</sub> measurements using the new UV Ozone Mapping and Profiler Suite (OMPS) Nadir Mapper (NM) instrument, launched into orbit on October 28, 2011 onboard the Suomi National Polar-orbiting Partnership (SNPP) spacecraft. We describe the first observations of SO<sub>2</sub> from SNPP/OMPS, quantify the daily loadings, estimate the spatial extent, and characterize the evolution of the January 2013 air pollution events over China.

## 2. Retrievals from OMPS NM

Suomi NPP/OMPS NM is a nadir-viewing hyper-spectral instrument that measures back-scattered ultraviolet (BUV) radiance spectra in the 300–380 nm wavelength range at a resolution of 1 nm (defined as the full width at half maximum (FWHM) of the spectral response function) and a sampling rate of 2.4 pixels per FWHM. It is in a Sun-synchronous, low Earth orbit, with a local ascending (northbound) equator crossing time at 1:30 pm. Contiguous daily global coverage is delivered using a two-dimensional Charge Coupled Device (CCD) detector array that covers a 2800 km cross-track swath (110° Field Of View, FOV) with a nadir pixel size of 50 km × 50 km, attributed to the heritage of the Total

Ozone Mapping Spectrometer (TOMS) missions [*Heath et al.*, 1975; *Fleig et al.*, 1982].

The improved performance of OMPS NM includes high signal-to-noise ratio (e.g.,  $\sim 1500$  at 310 nm) radiance measurements using a single detector array to cover the entire measured spectral range; hence it is uniquely suitable for SO<sub>2</sub> measurements. In contrast, the predecessors of OMPS NM, including the Global Ozone Monitoring Experiment (GOME) [*Burrows et al.*, 1999] on the European Remote Sensing Satellite-2 (ERS-2), the SCanning Imaging Absorption SpectroMeter for Atmospheric CHartographY (SCIAMACHY) on Environmental Satellite (ENVISAT) [*Bovensmann et al.*, 1999], the Ozone Monitoring Instrument (OMI) on Aura [*Levelt et al.*, 2006], and GOME2 [*Munro et al.*, 2006] on MetOp-A and B, measured earthshine radiance using three or more spectral channels to cover a broader wavelength range at higher sampling frequencies and narrower spectral resolutions. For SCIAMACHY, OMI, and GOME-2, there is a channel split near 310 nm.

Consequently the measured radiance spectra of these instruments in the channel-overlap region (extending a few nanometers either side of 310 nm) are degraded, and are in general not used in SO<sub>2</sub> retrievals, even though this region is highly sensitive to SO<sub>2</sub> in the PBL.

We also stress that OMPS NM is currently the only operational UV satellite instrument providing contiguous daily global coverage at low- to mid-latitudes, due to data gaps in the OMI and GOME-2 measurements.

To take advantage of the hyperspectral UV measurements and reduce the impact of measurement noise, in order to extract more reliable geophysical information, we refine and apply the iterative spectral fitting (ISF) algorithm developed by Yang et. al. [2009, 2010] to OMPS NM radiance spectra between 308 and 345 nm. This spectral range is

divided into two sub-windows in the iterative fitting process, 308–333 nm and 333–345 nm.

The former is used to derive the amounts of O<sub>3</sub> and SO<sub>2</sub> constrained by the respective climatological O<sub>3</sub> [Bhartia and Wellemeyer, 2002] and SO<sub>2</sub> [Lee *et al.*, 2009] profiles, while the latter is used for determination of spectral surface reflectivity or cloud fraction.

Specifically, we use the Mixed Lambert-Equivalent Reflectivity (MLER) model [Ahmad *et al.*, 2004] to account for the effects of partial cloud and/or aerosol detected in the OMPS instantaneous FOV (IFOV), and the MLER cloud pressure is simultaneously retrieved by adjusting it until the calculated Rotational Raman Scattering (RRS) filling-in factor [Joiner *et al.*, 1995] matches the corresponding measurement. This pressure is usually lower than that of the ground surface, and represents the level of an opaque surface that reproduces the combined reflection of the ground surface and scattering particles (clouds and/or aerosols) in the atmosphere. The lower the MLER pressure, the higher the altitude of these scattering particles in the atmosphere. Using this simultaneously derived cloud pressure and cloud fraction facilitates the proper treatment of the partial shielding of trace gases located below the scattering particles, as well as the enhancement of trace gases located at higher altitudes.

The precision of the PBL SO<sub>2</sub> data from the OMPS ISF retrieval is about 0.2 Dobson Units (DU; 1 DU =  $2.69 \times 10^{16}$  molecules/cm<sup>2</sup>), estimated from the standard deviation of background SO<sub>2</sub> measurements. However it is more difficult to quantify the ISF SO<sub>2</sub> retrieval accuracy, which is mainly determined by two factors: the vertical distribution of SO<sub>2</sub> and the presence of cloud and/or aerosol. A mismatch between the climatological and the true SO<sub>2</sub> profiles, as well as a difference in the modeled and the actual mean paths of

photons backscattered to the satellite sensor, can lead to retrieval errors, especially in the presence of cloud and/or aerosols. The ISF retrieval using OMI data has been validated against in situ aircraft measurements in China [He *et al.*, 2012]. It was found that ISF retrievals yield accurate quantification of SO<sub>2</sub> when the concentration is high, and is more accurate than retrievals using the band residual difference (BRD) method [Krotkov *et al.*, 2006]. Frequently the mass loading of a geographic region is aggregated from many satellite IFOVs. In this case, because the errors associated from profile shape assumptions and cloud/aerosol effects may cancel out in the summation, the uncertainty in the total is usually much smaller than that of the individual measurements, and is estimated to be less than 10% when the total SO<sub>2</sub> mass loading is greater than 10 kilotons (kt).

In addition to O<sub>3</sub> and SO<sub>2</sub> columns, the ISF retrieval provides useful information on atmospheric conditions and the underlying surface at the time of observation. The UV Aerosol index (AI), proportional to the slope of spectral reflectivity [Yang *et al.*, 2009 and 2010] in an IFOV, is also obtained from the retrieved MLER parameters. A positive AI value indicates the presence of UV absorbing aerosols: dust, smoke, or both. Thus UV satellite measurements can potentially provide coincident information on O<sub>3</sub>, SO<sub>2</sub>, NO<sub>2</sub> and particulate matter, which represent four of the six Criteria air pollutants identified by the US Environmental Protection Agency (EPA).

### **3. Results: SO<sub>2</sub> and Smog Episodes**

The wealth of information retrieved from OMPS NM measurements, and its daily global coverage, provide a unique synoptic perspective on episodic air pollution events. Here, we

demonstrate this capability of monitoring global atmospheric environments with the first quantification of air pollution over China in January 2013.

The air quality related geophysical parameters are displayed in Figure 1, which show maps of SO<sub>2</sub> vertical column density (VCD) in DU and AI over East Asia, retrieved from OMPS observations for three days in January 2013. The SO<sub>2</sub> maps reveal the spatial distribution of this air pollutant, one of the main components of smog. Similarly the AI maps (Figure 1, panels d-f) display the geographic distribution of UV-absorbing aerosols. These patterns suggest that both local aerosols (smoke and urban/industrial aerosols) and dust blown from the Taklimakan and Gobi deserts of western China contribute to the aerosol load in eastern China. The three days selected for Figure 1 represent dates with heavy (panel a), light (panel b), and moderate (panel c) SO<sub>2</sub> loadings. For the day with a high loading, the map (panel a) shows the widespread distribution of SO<sub>2</sub>, blanketing a large portion of eastern China; a high-pressure system (Figure 1g) that suppressed atmospheric dispersion in the region likely contributed to heavy smog. In contrast, on the days with medium and low loadings, hot spots of air pollution remain, such as in the Sichuan Basin and Beijing area (surrounded by mountains to the west, north, and northeast). These hot spots occurred persistently during this month, indicating the strength of local sources and/or effects of local topography and meteorology. However, under the synoptic conditions that are dominated by the mid-latitude trough (Figure 1h and i), large-scale high loadings of SO<sub>2</sub> are unlikely to occur. The maps also reveal the typical trajectories of air pollution outflow: the northeast flow path (Figure 1b) via

high mid-latitude large eddy systems and the east flow path (Figure 1c) via the prevalent subtropical-mid-latitude westerly winds.

To chart the evolution of air pollution in January 2013, we show in Figure 2 the daily SO<sub>2</sub> loadings (panel a), the extent of heavily SO<sub>2</sub> polluted areas (panel b, full bars) and smog-covered areas (panel b, sub (red) bars). The smog-covered areas are subsets of heavily SO<sub>2</sub> (>0.5 DU) polluted regions, in which the UV AI is also high (>1). The time series in Figure 2 shows four distinctive, synoptic-scale air pollution episodes. The first one was the longest, lasting for 12 days from the beginning of January. During the first episode, high SO<sub>2</sub> loadings, often mixed with high levels of UV-absorbing aerosols, covered a large portion of eastern China. Additional large-scale episodes occurred on Jan. 14 to 16, Jan. 21 to 24 and from Jan. 28 to 30, respectively. There was a more localized smog episode, affecting the Beijing and Tianjin regions and their vicinity, which occurred on the 18th and the 19th of January.

Daily satellite observations provide snapshots of SO<sub>2</sub> spatial distributions, not only influenced by the source of emissions, but also strongly affected by the local meteorological conditions and topography. The recurrent satellite overpasses allow time-averaging of these instantaneous measurements, yielding a stable spatial distribution that relates more closely to the locations and fluxes of the emission sources [*Fioletov et al.*, 2011]. Figure 3a shows the average SO<sub>2</sub> VCD map derived from OMPS NM observations with less than 50% cloud cover (i.e., MLER cloud fraction <0.5) in the IFOVs over East Asia for January 2013. The highest average OMPS VCDs (>1 DU) are all located just south and southeast of Beijing, distributed within three provinces (Shandong, Hebei, and Henan),

indicating that SO<sub>2</sub> emissions from these provinces are the major contributors to air pollution in January. These high concentrations of SO<sub>2</sub> were likely intensified by synoptic anomalies, including a weaker Siberian high and a localized high-pressure anomaly over northeast China (Figure 3c), which resulted in persistent higher relative humidity, higher temperature, and weaker winds that favor the formation of smog. Moderately elevated SO<sub>2</sub> concentrations are also evident in Liaoning, Jiangsu, Shanxi, and Sichuan/Chongqing provinces, signifying the locations of additional sources of air pollutants. Lastly, isolated and low-level enhancements of SO<sub>2</sub> above the background are detected in Hubei province, Ningxia Region, and Urumqi in Xinjiang Region, representing weaker emissions sources that contributed to the widespread distribution of these air pollution episodes.

To evaluate the OMPS SO<sub>2</sub> retrievals, we show in Figure 3b the corresponding average OMI SO<sub>2</sub> map, derived from the lower tropospheric (TRL) SO<sub>2</sub> VCDs (ColumnAmountSO2\_TRL in the operational OMI product, OMSO2). The OMI TRL SO<sub>2</sub> VCDs are derived using the linear fit (LF) algorithm [Yang *et al.*, 2007], with a near uniform *a priori* SO<sub>2</sub> profile from the ground to about 5.5 km above sea level. Similar spatial distributions of elevated SO<sub>2</sub> are exhibited in panels (a) and (b) of Figure 3, with the OMI TRL SO<sub>2</sub> VCDs mostly lower than the corresponding OMPS ISF values. The lower TRL SO<sub>2</sub> columns are expected due to the generally higher center of mass of the *a priori* profiles relative to the climatological profiles [Lee *et al.*, 2009] used in OMPS ISF retrievals. This comparison also shows that OMI detects more of the SO<sub>2</sub> transport away from the sources, as illustrated in Figure 3b with elevated SO<sub>2</sub> values distributed further east, away from the coast of China, primarily due to OMI's smaller pixel sizes that are more capable of

seeing through broken clouds. These consistent spatial distributions of SO<sub>2</sub>, obtained using different (ISF and LF) algorithms from independent satellite measurements, provides an indirect validation of the new OMPS NM retrievals.

#### 4. Summary

We have shown that OMPS NM provides high quality PBL SO<sub>2</sub> measurements, characterized by low biases (within  $\pm 0.2$  DU) in both along- and cross-track directions of the orbital swaths, and by high precision ( $\sim 0.2$  DU) for its IFOVs. The OMPS measurements are about seven times more precise than the current operational OMI PBL SO<sub>2</sub> retrievals, which have a  $\sim 1.5$  DU noise level [Krotkov *et al.*, 2008]. The improved SO<sub>2</sub> measurements are made possible by the unique instrument design that provide high quality spectral coverage of the 300 – 380 nm range using a single CCD detector array and by the stable instrument performance. Both the design and performance facilitate the accurate characterization and effective stray-light corrections of its hyper-spectral radiance measurements, which in turn allow the ISF algorithm to take advantage of the high SO<sub>2</sub> sensitivity region below 310 nm. The broader consistent high-quality spectral coverage, coupled with advances in retrieval algorithm and radiance correction techniques, now permit daily global observation of SO<sub>2</sub>, with an improved detection limit (precision of  $\sim 0.2$  DU) for SO<sub>2</sub> in the PBL for its IFOVs. The OMPS NM measurements can detect and quantify much smaller SO<sub>2</sub> amounts ( $\sim 0.01$  DU) with enhanced spatial resolution when averaging the repeated samplings of the same region over time. These improved measurements allow more accurate quantification of atmospheric SO<sub>2</sub> from volcanic emissions and

anthropogenic pollution to provide new information on the relative importance of these sources for climate studies.

Using the high quality OMPS data, we were able to quantify synoptic scale air pollution events over China in January 2013. The cumulative SO<sub>2</sub> mass measured by OMPS is 1065 kt ( $=1.065 \times 10^{12}$  g = 1.065 Tg). This represents the lower limit of total SO<sub>2</sub> loading within the bounding box (23.1°×23.1° dashed box in Figure 1) for this month, as SO<sub>2</sub> obscured from the satellite FOV by thick clouds and emissions on Sundays (on which OMPS operates in a mode with reduced spectral coverage) are not measured. This observed SO<sub>2</sub> mass is about half of the total SO<sub>2</sub> emission ( $\sim 2$  Tg [Yang *et al.*, 2010]) from the 2008 Kasatochi eruption (among the largest in the past decade), highlighting that coal combustion in China continues releasing large amounts of SO<sub>2</sub> into the atmosphere, and contributes greatly to the country's air pollution today.

The OMPS NM is designed primarily for measuring O<sub>3</sub> in the upper atmosphere. As demonstrated here, this well-characterized hyper-spectral instrument also provides sensitive observations of trace gases in the PBL. We are developing new capabilities to extract greater and more accurate information from these observations, so that the quality of OMPS trace gas products is sufficient to match or surpass those of the Aura/OMI environmental data records (EDR). We are on track to achieve this goal, as the next OMPS NM instruments, with an enhanced spatial resolution (12 km × 12 km at nadir), will fly on the NOAA and NASA Joint Polar Satellite System (JPSS) spacecraft: JPSS-1 (scheduled to launch in early 2017) and JPSS-2.

**Acknowledgments.** This work is supported by NASA under grant NNX11AK95G (Continuation of Long-Term Sulfur Dioxide EDR with the SNPP/OMPS NM). We acknowledge the use of OMPS Level 1B data produced by the SNPP Ozone Product Evaluation and Algorithm Test Element (PEATE), funded by NASA.

## References

- Ahmad, Z., P. K. Bhartia, and N. Krotkov (2004), Spectral properties of UV radiation in cloudy atmospheres, *J. Geophys. Res.*, *109*, D01201, doi: 10.1029/2003JD003395.
- Bhartia, P. K., and C. W. Wellemeyer (2002), OMI TOMS-V8 Total O<sub>3</sub> Algorithm, *Algorithm Theoretical Baseline Document: OMI Ozone Products*, edited by P. K. Bhartia, vol. II, ATBD-OMI-02, ver. 2.0. (Available at [ftp://jwocky.gsfc.nasa.gov/pub/LLM\\_climatology](ftp://jwocky.gsfc.nasa.gov/pub/LLM_climatology)).
- Bovensmann, H., J. P. Burrows, M. Buchwitz, J. Frerick, S. Noël, V. V. Rozanov, K. V. Chance, A. P. H. Goede (1999), SCIAMACHY: Mission Objectives and Measurement Modes, *J. Atmos. Sci.*, *56*, 127–150. doi: 10.1175/1520-0469(1999)056<0127:SMOAMM>2.0.CO;2.
- Burrows, John P., and Coauthors (1999), The Global Ozone Monitoring Experiment (GOME): Mission Concept and First Scientific Results, *J. Atmos. Sci.*, *56*, 151–175, doi: 10.1175/1520-0469(1999)056<0151:TGOMEG>2.0.CO;2.
- Carn, S. A., A. J. Krueger, N. A. Krotkov, K. Yang, and P. F. Levelt (2007), Sulfur dioxide emissions from Peruvian copper smelters detected by the Ozone Monitoring Instrument, *Geophys. Res. Lett.*, *34*, L09801, doi:10.1029/2006GL029020.

- Eisinger, M., and J. P. Burrows (1998), Tropospheric Sulfur Dioxide observed by the ERS-2 GOME Instrument, *Geophys. Res. Lett.*, *25*, 4177–4180, doi: 10.1029/1998GL900128.
- Dickerson, R. R., et al. (2007), Aircraft observations of dust and pollutants over northeast China: Insight into the meteorological mechanisms of transport, *J. Geophys. Res.*, *112*, D24S90, doi:10.1029/2007JD008999.
- Fioletov, V. E., C. A. McLinden, N. Krotkov, M. D. Moran, and K. Yang (2011), Estimation of SO<sub>2</sub> emissions using OMI retrievals, *Geophys. Res. Lett.*, *38*, L21811, doi:10.1029/2011GL049402.
- Fleig, A. J., K. F. Klenk, P. K. Bhartia, D. Gordon (1982), *NASA Ref. Publ.* RP 1096.
- Haagen-Smit, A. J. (1952), Chemistry and physiology of Los Angeles smog, *Ind. Eng. Chem.*, *44*(6), 1342–1346, doi: 10.1021/ie50510a045.
- He, Kebin, Hong Huo, and Qiang Zhang (2002), URBAN AIR POLLUTION IN CHINA: Current Status, Characteristics, and Progress, *Annu. Rev. Energy Environ.*, *27*:397–431, doi: 10.1146/annurev.energy.27.122001.083421.
- He, H., et al. (2012), SO<sub>2</sub> over central China: Measurements, numerical simulations and the tropospheric sulfur budget, *J. Geophys. Res.*, *117*, D00K37, doi: 10.1029/2011JD016473.
- Heath, D.F., A. J. Krueger, H. A. Roeder, B. D. Henderson (1975), *Opt. Eng.*, *14*(4), 144323, doi: 10.1117/12.7971839.
- Hsu, N. C., C. Li, N. A. Krotkov, Q. Liang, K. Yang, and S.-C. Tsay (2012), Rapid transpacific transport in autumn observed by the A-train satellites, *J. Geophys. Res.*, *117*, D06312, doi: 10.1029/2011JD016626.

Joiner J., P.K. Bhartia, R.P. Cebula, E. Hilsenrath, R.D. McPeters, and H.-W. Park (1995), Rotational-Raman scattering (Ring effect) in satellite backscatter ultraviolet measurements, *Appl. Optics*, *34*, 4513–4525, doi: 10.1364/AO.34.004513.

Krotkov, N.A., S.A. Carn, A.J. Krueger, P.K. Bhartia, and K. Yang (2006), Band residual difference algorithm for retrieval of SO<sub>2</sub> from the Aura Ozone Monitoring Instrument (OMI), *IEEE T. Geosci. Remote Sens.*, *44*(5), 1259–1266, doi: 10.1109/TGRS.2005.861932.

Krotkov, N. A., et al. (2008), Validation of SO<sub>2</sub> retrievals from the Ozone Monitoring Instrument over NE China, *J. Geophys. Res.*, *113*, D16S40, doi:10.1029/2007JD008818.

Lee, C., A. Richter, M. Weber, and J. P. Burrows (2008), SO<sub>2</sub> retrieval from SCIAMACHY using the Weighting Function DOAS (WFDOAS) technique: Comparison with standard DOAS retrieval, *Atmos. Chem. Phys.*, *8*, 6137–6145, doi: 10.5194/acp-8-6137-2008.

Lee, C., R. V. Martin, A. van Donkelaar, G. O'Byrne, N. Krotkov, A. Richter, L. G. Huey, and J. S. Holloway (2009), Retrieval of vertical columns of sulfur dioxide from SCIAMACHY and OMI: Air mass factor algorithm development, validation, and error analysis, *J. Geophys. Res.*, *114*, D22303, doi: 10.1029/2009JD012123.

Levelt, P. F., G. H. J. van den Oord, M. R. Dobber, A. Mälkki, H. Visser, J. de Vries, P. Stammes, J. O. V. Lundell, and H. Saari (2006), The Ozone Monitoring Instrument, *IEEE Trans. Geosci. Remote Sens.*, *44*(5), 1093–1101, doi: 10.1109/TGRS.2006.872333.

Munro, R., M. Eisinger, C. Anderson, J. Callies, E. Corpaccioli, R. Lang, A. Lefebvre, Y. Livschitz, and A. Perez Albinana (2006), GOME-2 on MetOp, paper presented at

the 2006 EUMETSAT Meteorological Satellite Conference, Eur. Org. for the Exploit. of Meteorol. Satell., Helsinki.

Nowlan, C. R., X. Liu, K. Chance, Z. Cai, T. P. Kurosu, C. Lee, and R. V. Martin (2011), Retrievals of sulfur dioxide from the Global Ozone Monitoring Experiment 2 (GOME2) using an optimal estimation approach: Algorithm and initial validation, *J. Geophys. Res.*, *116*, D18301, doi: 10.1029/2011JD015808.

Tao, M., L. Chen, L. Su, and J. Tao (2012), Satellite observation of regional haze pollution over the North China Plain, *J. Geophys. Res.*, *117*, D12203, doi:10.1029/2012JD017915.

Thorsheim, P. (2009), *Inventing Pollution: Coal, Smoke, and Culture in Britain since 1800* (Ecology & History), Ohio University Press, Jun 15, 2009.

U.S. Energy Information Administration (2012), China Report, September 4, 2012, available on the web: <http://www.eia.gov/countries/analysisbriefs/China/china.pdf>.

Wang, J., X. Xia, P. Wang, and S. A. Christopher (2004), Diurnal variability of dust aerosol optical thickness and Angstrom exponent over dust source regions in China, *Geophys. Res. Lett.*, *31*, L08107, doi: 10.1029/2004GL019580.

Yang, K., N. A. Krotkov, A. J. Krueger, S. A. Carn, P. K. Bhartia, and P. F. Levelt (2007), Retrieval of large volcanic SO<sub>2</sub> columns from the Aura Ozone Monitoring Instrument: Comparison and limitations, *J. Geophys. Res.*, *112*, D24S43, doi:10.1029/2007JD008825.

Yang, K., N. A. Krotkov, A. J. Krueger, S. A. Carn, P. K. Bhartia, and P. F. Levelt (2009), Improving retrieval of volcanic sulfur dioxide from BUUV satellite observations, *Geophys. Res. Lett.*, *36*, L03102, doi: 10.1029/2008GL036036.

Yang, K., X. Liu, P. K. Bhartia, N. A. Krotkov, S. A. Carn, E. J. Hughes, A. J. Krueger,  
R. J. D. Spurr, and S. G. Trahan (2010), Direct retrieval of sulfur dioxide amount and  
altitude from spaceborne hyperspectral UV measurements: Theory and application, *J.*  
*Geophys. Res.*, 115, D00L09, doi: 10.1029/2010JD013982.

Accepted Article

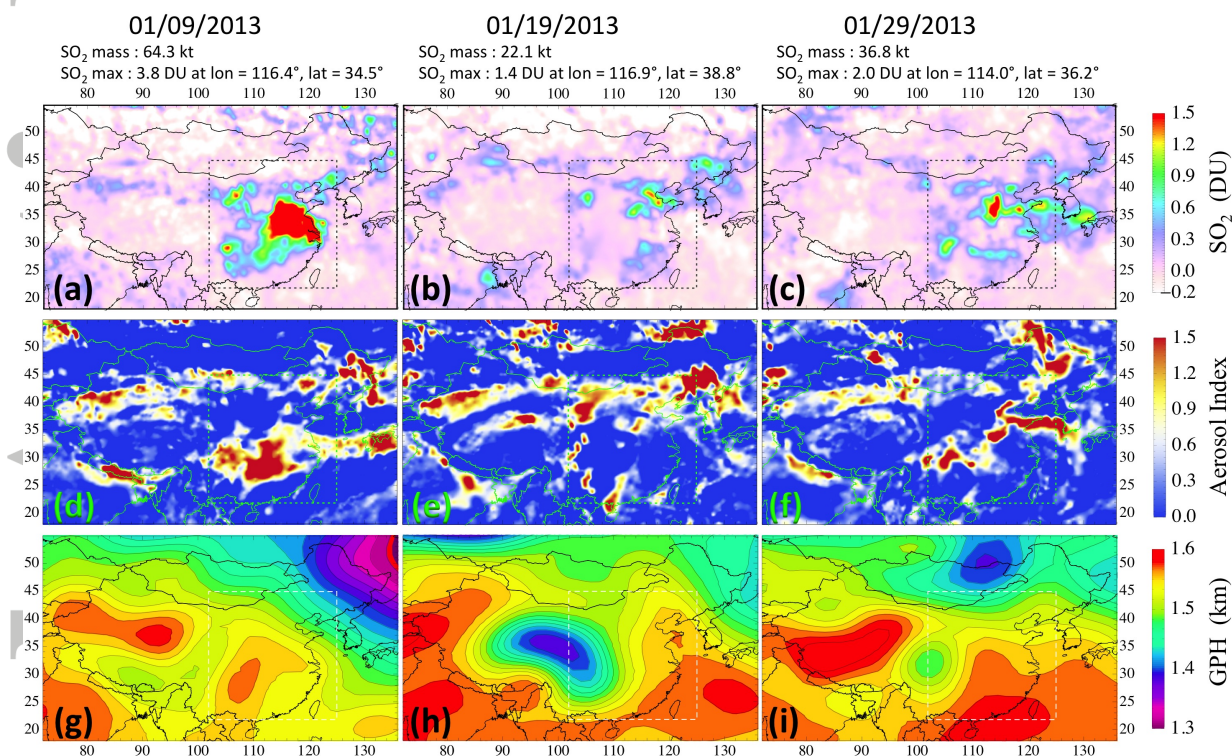


**Figure 1.** Maps of SO<sub>2</sub> vertical column (VCD) density and aerosol index (AI) from OMPS ISF retrievals for three days in January 2013. The SO<sub>2</sub> loading, maximum SO<sub>2</sub> VCD, and its corresponding location are displayed above each SO<sub>2</sub> map (a-c). The loading is computed as the total SO<sub>2</sub> mass observed within the dashed square area on the map, with lower left corner at (101.9°E, 21.8°N) and the upper right corner at (125.0°E and 44.9°N). Panels (g-i) are the NCEP reanalysis 850 hPa geopotential height (GPH in km) at 0600 UTC for these three days. Note that the full swaths of the OMPS observations are used in producing these daily maps, without filtering based on surface albedo, cloud fraction, or viewing angles. Only a few pixels with low retrieval quality are excluded from the maps.

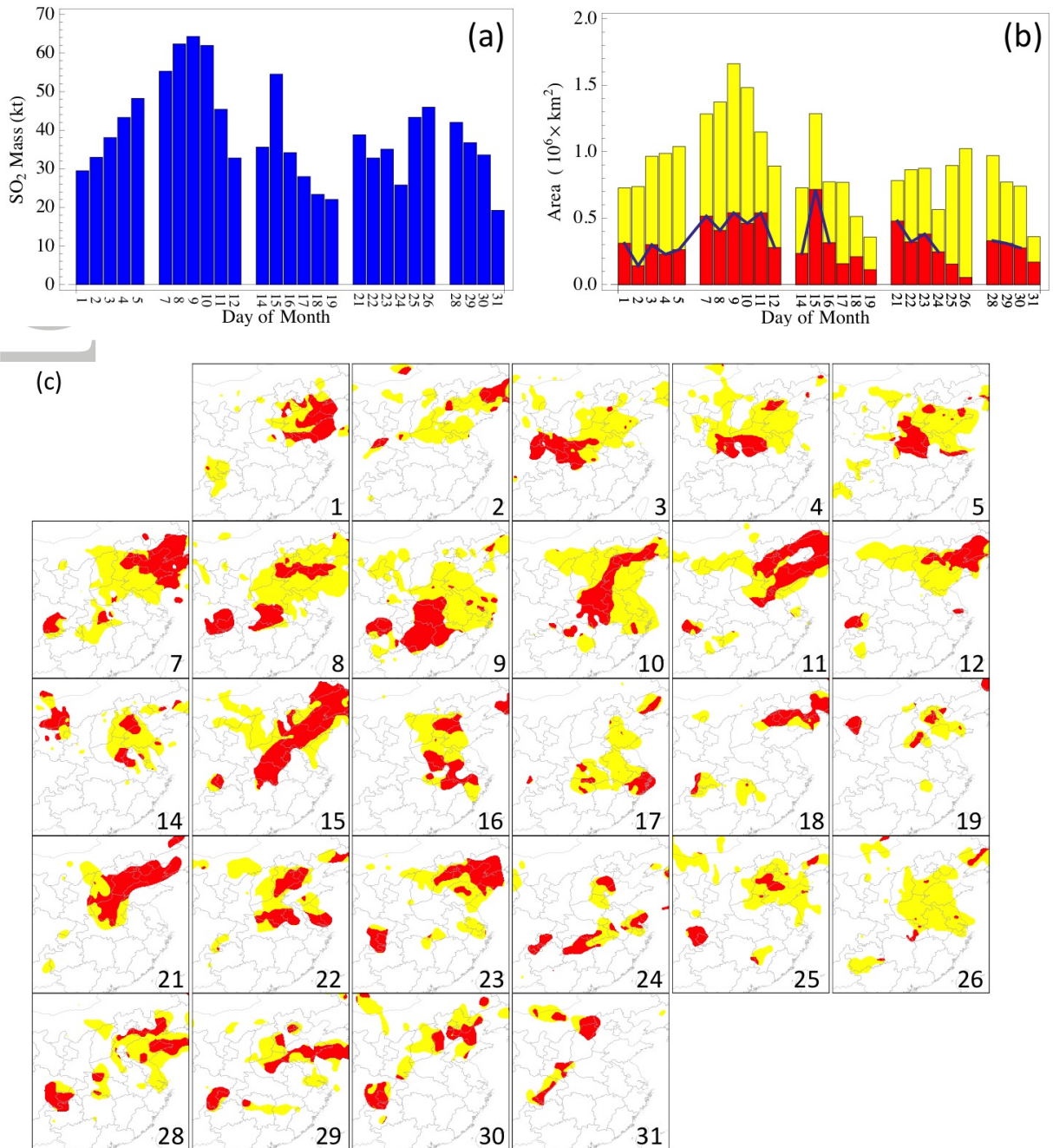


**Figure 2.** (a) observed SO<sub>2</sub> masses (kilotons), and (b) SO<sub>2</sub> covered areas (million square kilometers) within the square-bounding box shown in Figure 1, for each day (except Sunday) in January 2013. Results on Sundays are not shown, because OMPS NM is operated in a high-spatial resolution mode, with a reduced spectral coverage. The daily mass is the sum of all SO<sub>2</sub> values in the bounding box for the day, but areas are calculated for high SO<sub>2</sub> (>0.5 DU) regions, i.e., the sum of the yellow and red zones in the corresponding map in (c). The red zones are defined as smog-covered areas, in which both SO<sub>2</sub> and the UV aerosol index (AI) are high (i.e., SO<sub>2</sub> > 0.5 DU and AI > 1), and the yellow zones are high SO<sub>2</sub> and low AI areas (SO<sub>2</sub> > 0.5 DU and AI < 1).

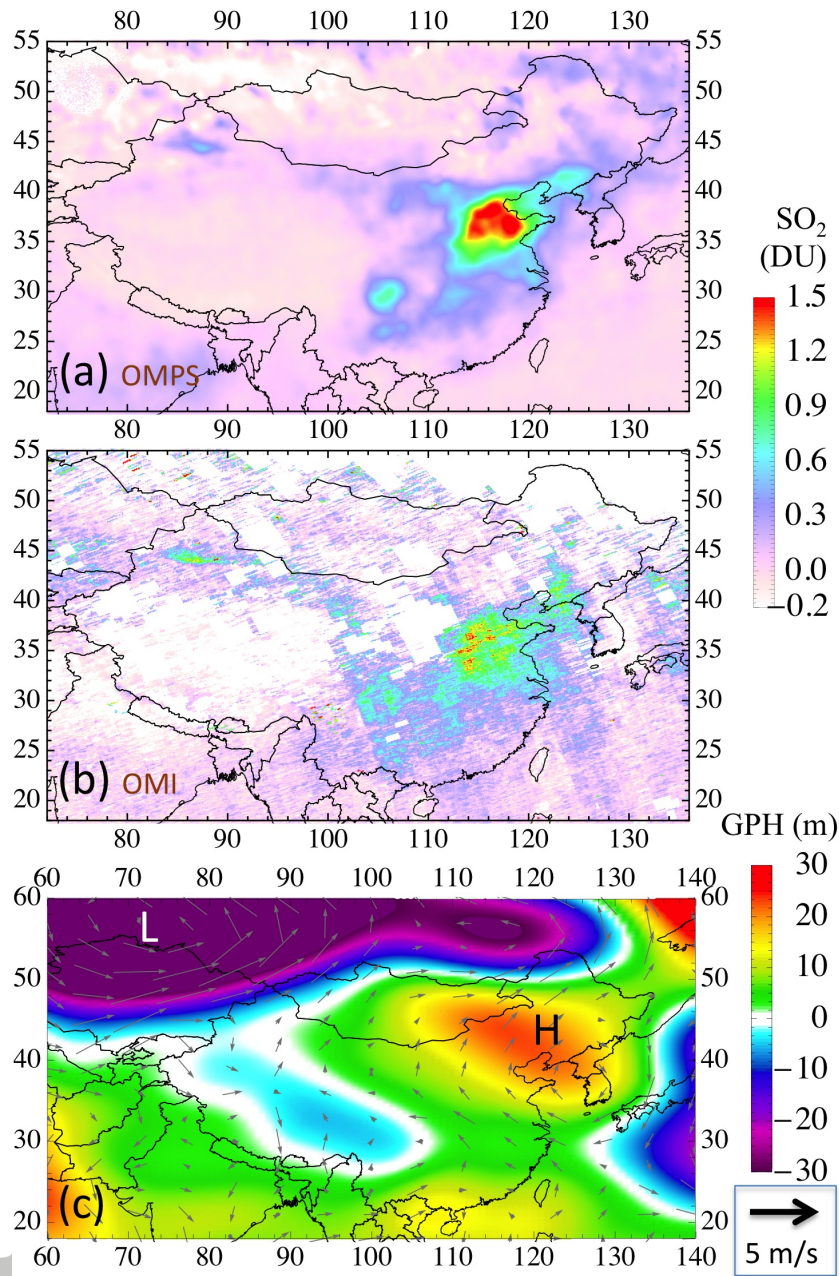


**Figure 3.** (a) Average SO<sub>2</sub> VCD map measured by SNPP/OMPS NM with MLER cloud fraction less than 50% over East Asia for January 2013; (b) The corresponding SO<sub>2</sub> map composited with the lower tropospheric SO<sub>2</sub> column (ColumnAmountSO2.TRL) of the operational OMI SO<sub>2</sub> product; (c) 500 hPa geopotential height (GPH) anomaly and 700 hPa wind vector anomaly (with respect to the 1980-2010 means) for Jan 2013. Letters ‘L’ and ‘H’ respectively indicate the negative and positive geopotential anomalies. The highest OMPS SO<sub>2</sub> VCD is 1.65 DU, located at (118.3°E, 36.8°N), and the OMI SO<sub>2</sub> VCD is 0.8 DU at this location. Note that the OMPS map includes observations from its full swath, while the OMI map (panel b) is produced with cross-track samples 1 to 21 (out of 1 to 60) to avoid the effect of the row anomaly (see <http://www.knmi.nl/omi/research/product/rowanomaly-background.php>).